Hindawi
Advances in Meteorology
Volume 2019, Article ID 8613943, 14 pages
https://doi.org/10.1155/2019/8613943

Research Article

Measuring Radial and Tangential Changes in Tropical Cyclone Rain Fields Using Metrics of Dispersion and Closure

Corene Matyas[1] **and Jingyin Tang**[2]

[1]*Department of Geography, University of Florida, Gainesville, Florida 32611, USA*
[2]*IBM, 1001 Summit Blvd, Brookhaven, GA 30319, USA*

Correspondence should be addressed to Corene Matyas; matyas@ufl.edu

Received 16 December 2018; Revised 1 March 2019; Accepted 3 March 2019; Published 1 April 2019

Academic Editor: Tomeu Rigo

Although tropical cyclone (TC) rain fields assume varying spatial configurations, many studies only use areal coverage to compare TCs. To provide additional spatial information, this study calculates metrics of closure, or the tangential completeness of reflectivity regions surrounding the circulation center, and dispersion, or the spread of reflectivity outwards from the storm center. Two hurricanes that encountered different conditions after landfall are compared. Humberto (2007) experienced rapid intensification (RI), stronger vertical wind shear, and more moisture than Jeanne (2004), which was more intense, weakened gradually, and became extratropical. A GIS framework was used to convert radar reflectivity regions into polygons and measure their area, closure, and dispersion. Closure corresponded most closely to storm intensity, as the eye became exposed when both TCs weakened to tropical storm intensity. Dispersion increased by 10 $km \cdot hr^{-1}$ as both TCs developed precipitation along frontal boundaries. As closure tended to change earlier than dispersion and area, closure may be most sensitive to subtle changes in environmental conditions, particularly as the storm's core experiences the entrainment of dry air and erodes. Displacement provided a combined radial and tangential component to the location of the rainfall regions to confirm placement along the frontal boundaries. Examining area alone cannot reveal these patterns. The spatial metrics reveal changes in TC structure, such as the lag between onset of RI and maximum closure, which should be generalizable to TCs experiencing similar conditions. Future work will calculate these metrics for additional TCs to quantify structural changes in response to their surrounding environment.

1. Introduction

The rainfall produced by tropical cyclones (TCs) can cause devastating floods as recently witnessed during hurricanes Harvey (2017) and Florence (2018). According to Rappaport [1] , more people die in floods induced by rainfall from TCs than any other TC-related hazard when examined on a per-storm basis. Thus, researchers are continually motivated to better model the processes that contribute to the development of intense precipitation within TCs and where precipitation is produced within the storm so that rainfall forecasts can be improved [2–4].

One popular method of comparing rainfall regions among multiple storms is to examine areal coverage [2, 5–7]. However, areal coverage does not provide information about the spatial distribution of rainfall regions. Configurations of TC rain fields can vary according to environmental conditions and storm attributes. Intense TCs moving through environments that are high in moisture with low vertical wind shear are symmetric with rainfall encircling the storm center [8, 9]. When vertical wind shear is large, TCs develop wavenumber-1 asymmetries in rainfall as most convection occurs in the downshear quadrants [10–13]. While TCs embedded in moist environments can be larger [14, 15] and environments that are more dry can limit storm size [16, 17], the entrainment of dry air introduces asymmetries in rainband configurations [18–20]. As the wind circulation weakens after landfall, convergence into the circulation center decreases, which allows entrainment of relatively dry continental air masses into the storm's core. Interaction

with the middle-latitude westerlies and associated troughs can lead to extratropical transition during which rainfall decreases on the equatorward side of the storm but increases on the poleward side of the storm [21, 22]. Weakening after landfall, increasing vertical wind shear, reductions in moisture, and baroclinic interactions should lead to less rainfall surrounding the circulation center (decreasing closure) and spreading of rainfall away from the storm center (increasing dispersion).

One approach to analyzing TC rain fields is to consider the spatial distribution of the rainbands. The Dvorak technique [23, 24] uses satellite imagery to estimate the current and future intensity of TCs through a set of curves related to intensity change and images of central features and outer banding features that correspond to each interval. Convective clouds with large stratiform regions on the edges surround the eyewall in a ring-like formation [25], which causes the central features seen on visible satellite images in Dvorak [23]. For the outer banding features, convection forms in a more cellular nature beyond ~200 km from the center [26]. The primary, or tangential [27], and secondary, or in, up, and out [28], wind circulations help to organize the configuration of TC rainbands. The inner and outer regions of the primary circulation may be controlled by different physical mechanisms [29, 30], which may explain why cloud development can differ in the inner vs outer regions of a TC.

Given that the primary and secondary circulations in a TC weaken after landfall, the resulting configuration of rainbands should also exhibit changes in the tangential and radial directions relative to the storm center. The storm's center should become increasingly exposed to the continental air mass as the tangential component of its circulation weakens, thereby decreasing the ability of rainfall regions to completely encircle the center, which decreases closure. Rainfall regions should decrease in coverage in the storm's core as its secondary circulation weakens but could increase in the outer regions due to interaction with frontal boundaries to become more dispersed rather than compact. However, the rates of change in closure and dispersion depend on storm intensity and size as well as the amount of moisture available and vertical wind shear that is encountered. Thus, the need exists to calculate the rates of change in TC rainband structures to better link their responses to changing environmental conditions and storm attributes.

This study uses the spatial metrics of closure and dispersion to compare tangential and radial components of rainband configurations in addition to areal coverage in two landfalling hurricanes that experience different conditions. We define rainfall regions using reflectivity values from the Weather Surveillance Radar 1988 Doppler (WSR-88D) network, given their high spatial and temporal resolution, and analyze the reflectivity regions using a geographic information system (GIS). Regions of lower (20 dBZ) and higher (40 dBZ) reflectivity are considered. Calculations of area, closure, and dispersion are made every 10 minutes. Additionally, we calculate displacement to provide a directional component to dispersion so that the location of rainfall can be quantified as these TCs encounter different atmospheric conditions. While we primarily analyze rainfall regions within 500 km of the storm center, we also employ multiple search radii to demonstrate that the method can be used to isolate different regions of a storm.

In this comparison study, we profile changes in the rain fields of Jeanne (2004), a major hurricane which eventually completed an extratropical transition, and Humberto (2007), which rapidly intensified but then dissipated after landfall. Different values and rates of change for closure, dispersion, and area should occur in each case. Jeanne and Humberto were selected for this study as they had key similarities, important differences, and presented unique opportunities for analysis. For data analysis purposes, both TCs were detected by the WSR-88D network during the legacy period when the spatial resolution for reflectivity data is 1 km by 1° [31] so that the spatial resolution of the observations is the same. According to Franklin et al. [32], Jeanne made landfall as a major hurricane over eastern Florida at 0400 UTC 26 September 2004. It weakened to a tropical storm 14 hours after landfall and then to a tropical depression 24 hours later while moving northward and interacting with a frontal zone. It was declared posttropical at 0000 UTC on 29 September. Humberto's development differed markedly as it formed close to land and experienced rapid intensification (RI) from a tropical depression into a hurricane before landfall at 0700 UTC 13 September 2007 [33]. Humberto spent less time over land compared to Jeanne, becoming a tropical depression by 0000 UTC 14 September and dissipating 18 hours later. As both storms reached their maximum intensity within an hour of landfall, our study should sample them at their most enclosed and compact configurations. However, differences in their spatial structure should be evident due to variations in intensity and evolution. Jeanne had a maximum sustained wind speed of 54 $m \cdot s^{-1}$ (105 kt) at landfall and had been a hurricane for more than five days. Jeanne also presents an opportunity for analysis over multiple days while weakening and transitioning into an extratropical cyclone. Humberto formed only 25 hours prior to landfall and underwent RI in six hours to achieve maximum sustained winds of 41 $m \cdot s^{-1}$ (80 kt) at landfall, providing an opportunity to measure changes in structure during this process that infrequently occurs near landfall [34].

2. Data and Methods

2.1. Spatial Analysis of Rainfall Regions. The spatial metrics utilize the position of the storm's circulation center in their calculation. Thus, we first obtain storm positions and intensity from the best track data [35]. However, the precision of the 6-hourly data is limited to 0.1°. As we require data at a higher temporal and spatial resolution, we perform a cubic spline interpolation to produce positions every 10 minutes. We inspect the new positions by overlaying them with the reflectivity values in a GIS to ensure that they are reasonable.

We next utilize a map-reduce framework [36] to process Level II reflectivity data from radars within 600 km of

the storm center. As detailed by Tang and Matyas [37], all inputs, intermediate results, and outputs are represented as key-value pairs. This allows us to chain multiple maps and reduce functions in a pipeline to operate on complex tasks in map-reduce jobs. The complete procedure includes four steps: preprocess, map function chain, reducing function chain, and postprocess. Preprocessing includes decompressing raw Level II data and applying quality control. In the map function chain, polar to Cartesian coordinate system conversion occurs, and data are gridded at 1 km × 1 km × 0.5 km resolution every 10 minutes using data from a 20-minute moving window. The reduction step includes calculations for weights applied when multiple reflectivity gates cross a single grid cell and interpolations to fill empty cells. Values for grid cells with data from multiple radars are calculated by retaining the highest value as shown by Steiner et al. [38] and Matyas et al. [19]. Cells with missing values are filled using a distance-weighted interpolation. Postprocessing is where results are written to disk. An in-depth description of these procedures, see [37].

We then define the regions of reflectivity that will undergo spatial analysis. We extract data from an altitude of 3.5 km (Figure 1(a)) and use a GIS to draw contours that enclose regions of reflectivity that are greater than or equal to 20 dBZ to represent lower rain-rate areas that define the edge of the storm and greater than or equal to 40 dBZ to represent regions of higher rain rates that could contain convective cells [19, 39]. The contours are converted into polygons (Figure 1(b)). For each polygon larger than 50 km^2, we calculate the center of mass and its distance from the TC's center. Many studies employ a 500 km search radius to identify rainfall belonging to a TC [40, 41]. Thus, we employ a 500 km search radius (Figure 1(c)) but include the entirety of polygons that have their centroid within this radius rather than truncating regions extending beyond this radius. We sum the areas of all 20 and 40 dBZ polygons separately to examine changes in area over time to make our results comparable to other studies.

Spatial metrics are then calculated to describe the tangential and radial properties of the reflectivity regions. As TC rainbands tend to curve due to the spiral nature of inflow into the system, we quantify the degree to which the storm center is enclosed by reflectivity values [19, 42]. Closure (equation (1)) is calculated by counting the number of 1° radials emanating from the circulation center out to 500 km that intersect with a polygon and dividing by 360 so that a value of 1 indicates complete closure while 0.5 indicates that only half of the arc contains reflectivity values:

$$C = \frac{\text{no. of } 1^\circ \text{ angles intersecting polygons}}{360}. \quad (1)$$

Dispersion (equation (2)) measures the radial distribution of reflectivity with respect to the circulation center. Values increase as the reflectivity region centroid(s) (r_{centroid}) move away from the circulation center and toward the search radius (r_{search}) of 500 km. Larger regions receive more weight in the calculation, and the final value is obtained by summing over all distinct reflectivity regions, with NP representing the number of polygons [9]. In this analysis, a value of one indicates that all polygon centroids are located along the edge of the 500 km search radius:

$$D = \sum_{i=1}^{NP} \frac{\text{area}_i}{\sum_j^{NP} \text{area}_j} \left(\frac{r_{\text{centroid},i}}{r_{\text{search}}} \right). \quad (2)$$

Prior to analysis, the area and metric values are smoothed using a 30-minute window. In general, closure should decrease after landfall due to the weakening of the primary circulation, dry air entrainment, and increasing vertical wind shear. Because Jeanne (2004) completed an extratropical transition, we expect it to lose convection within its inner core and its rain fields to expand poleward of the storm center [43–45] so that dispersion should generally increase. Humberto experienced RI prior to landfall; thus, its shape should become more compressed, meaning a decrease in dispersion [9]. However, the weakening of the secondary circulation should cause dispersion to increase thereafter.

2.2. Analysis of Environmental and Storm Conditions. We seek to connect changes in reflectivity to changes in the environment surrounding each TC as well as the storm intensity and size. Due to a relatively high spatial (32 km × 32 km) and temporal (3 h) resolution, we extract data for specific humidity and vertical wind shear from the North American Regional Reanalysis (NARR) [46]. Zick and Matyas [47] demonstrated that Jeanne and Humberto were well represented in this dataset. To summarize moisture and shear, we employ the same calculations as in the Statistical Hurricane Intensity Prediction Scheme [48], which produce areal averages by considering data 200–800 km from the storm center. Deep-layer vertical wind shear is calculated over 200–850 hPa. We calculate specific humidity over 900–1000 hPa to represent boundary layer, 700–850 hPa for low, 500–700 hPa for mid, and 300–500 hPa for high tropospheric conditions. Storm size and intensity are examined using the 6 h data from the extended best track dataset from the National Hurricane Center's operational estimates. It should be noted that unlike storm position and intensity, data pertaining to storm size do not undergo a postseason quality control. Specifically, we examine minimum central pressure, radius of maximum winds, radius of gale-force winds (R17) in each quadrant, and the radius of the outermost closed isobar (ROCI).

2.3. Statistical Analyses. The first set of statistical tests identify whether the storms had similar values of moisture, shear, intensity, size, area, closure, and dispersion. The Wilcoxon rank sum test [49] is nonparametric and compares two independent samples that have equal variance. The null hypothesis is that the samples have equal medians. If the test produces a p value less than 0.05, we reject the null hypothesis as the distribution of one population has higher values than the other. The data from the two storms are paired temporally by setting the time of landfall equal to zero. Only time periods when data from both storms are available are analyzed. For area and the spatial metrics, we analyze data until 12 hours after landfall and we also pair the

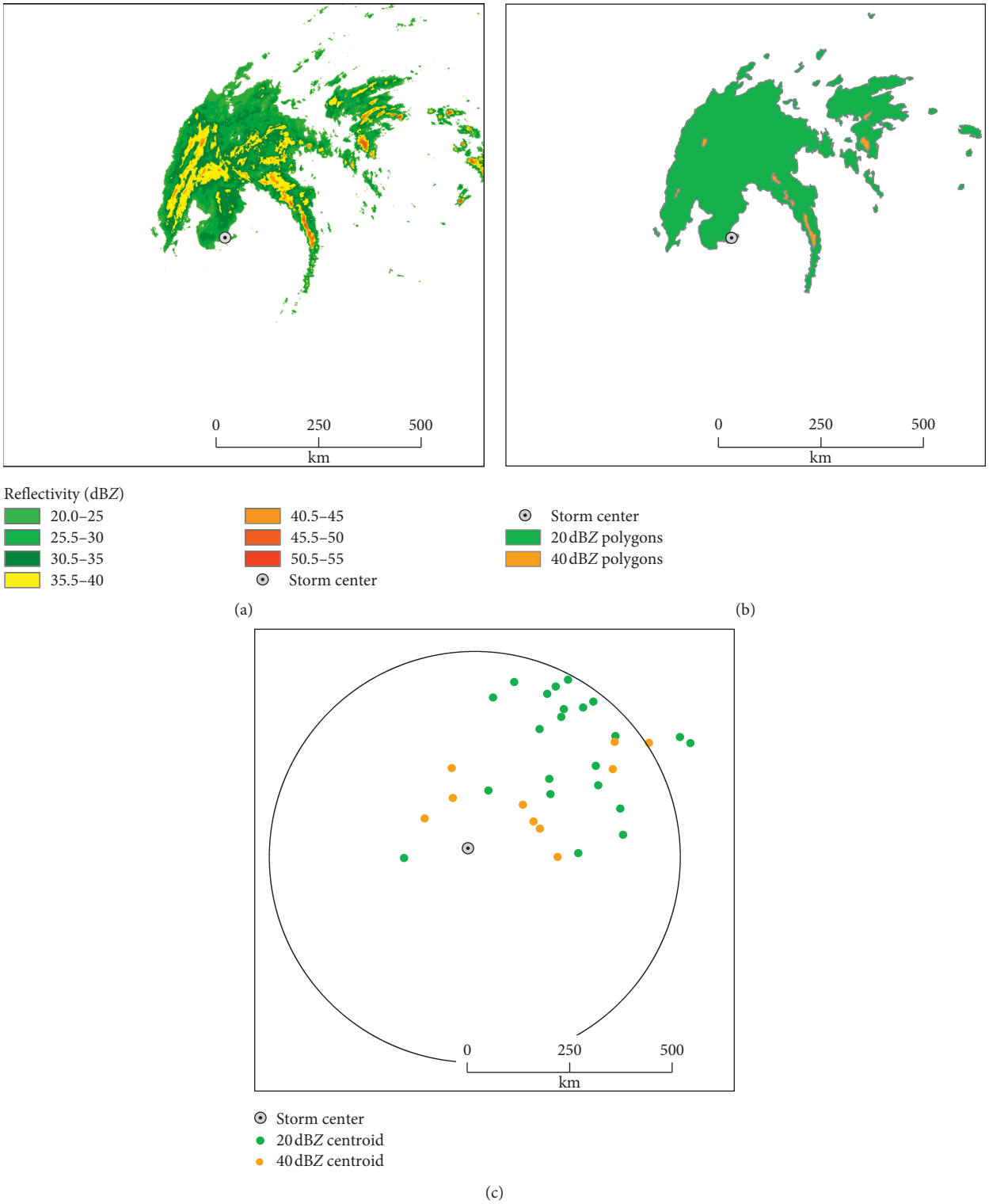

Figure 1: Hurricane Jeanne at 43 hours after landfall showing (a) mosaicked radar reflectivity values at 3.5 km altitude, (b) conversion of reflectivity values to polygons whose boundaries are used in the closure calculation, and (c) search radius of 500 km where polygon centroids within this distance are used for the dispersion calculation. At this time, 20 dBZ closure is 0.81 or 292° while 40 dBZ closure is 0.24 or 86°. Dispersion for 20 dBZ regions is 0.44 or 220 km, while for 40 dBZ regions, it is 0.50 or 250 km.

observations by setting as zero the last observation point for each storm and examine the prior twelve hours to compare the periods when frontal interaction occurred.

A set of Spearman's rank correlation coefficients are calculated to compare the values of dispersion, closure, and area to one another. As the primary and secondary

circulations of a TC are related, we also expect closure and dispersion to be related. Less area of reflectivity should correspond to lower values of closure, as polygons need to stretch around larger circles at more distant radii to produce a high closure value. The exception would be when large regions of rainfall formed in a linear pattern extending outwards from the circulation center as could happen during interaction with a frontal boundary instead of wrapping around the center. Dispersion increases when rainfall diminishes in the storm's core which should lower the area. However, the development of rainfall in the outer regions along a frontal boundary that stretches parallel to the tangential circulation could increase both dispersion and area.

Measuring correlation provides a general view of the relationship between variables. However, we also wish to look more closely at variations in the trends of the spatial metrics and the timing of when trends change. Thus, we utilize a change point analysis that searches each time series separately for up to four points where changes in trends occur. These change points must be at least four observations from either end of the time series and must have at least four observations in between. We calculate a trend line that best fits the observations between each change point and check its rate of change, converting values from the ranges of 0-1 to units of km·hr^{-1} for dispersion and hr^{-1} for closure to give a clearer physical interpretation of the results. To check the fit of each trend line to the observations, we calculate the coefficient of determination.

3. Results

3.1. Storm Size and Atmospheric Conditions. The results of the Wilcoxon rank sum tests for the atmospheric conditions (Table 1) confirm what is visible in Figure 2. While Humberto experienced much stronger vertical shear on average as compared to Jeanne, its surrounding environment also contained more moisture in the low, middle, and upper levels of the troposphere. Corbosiero and Molinari [10] classify vertical wind shear as being weak if below 5 m·s^{-1}. Although shear increased for both storms overall, Humberto's shear first exceeded 5 m·s^{-1} prior to landfall, while Jeanne's shear remained weak for a day after landfall. As shear limits the development of rainfall in the upshear quadrants and induces a tilt in the downshear direction [50, 51], dispersion should increase while closure may be limited to 0.5 or less for Humberto as it experiences stronger shear over its lifetime as strong shear is known to enhance convection in the downshear quadrants [10–13]. The direction of the shear differs between the two cases: westerly for Humberto and southwesterly for Jeanne. It is important to also consider moisture. While Jeanne has more moisture in the boundary layer, likely due to its location over the Florida peninsula at landfall, less moisture is available compared to Humberto in the mid to upper troposphere which may limit the support for deep convection. Thus, closure for 40 dBZ regions in Humberto may be higher than that for Jeanne if more 40 dBZ regions exist in Humberto.

As Jeanne was more intense than Humberto (Table 1), the stronger primary and secondary circulations should lead to rainfall completely surrounding the circulation center of Jeanne, yielding high closure, and the main rainfall region should surround the storm center so that its centroid is not greatly dispersed. Jeanne was also larger in size than Humberto (Table 1), with average ROCI of 370 km, R17 among all four quadrants of 224 km, and radius of maximum wind 72 km compared to 104, 30, and 22 km, respectively, for Humberto when nonzero values were present. These results are not surprising, given the long evolution of Jeanne compared with the short history of Humberto. According to the classification of TC size by Holland and Merrill [30], Jeanne was in the mature stage, which is when growth in size occurs. Humberto was either in the formative stage, which is when hurricane-force winds first develop or immature stage when rapid intensification occurs with minimal change in storm size. Given the larger size of Jeanne, more area exists over which rainfall could occur; thus, closure in the outer regions may be lower as it is more difficult for precipitation to completely encircle the storm center at large radial distances compared with smaller radial distances.

3.2. Reflectivity Regions. When examining the area occupied by reflectivity regions around landfall time, both storms had similar areas of 20 dBZ, but Humberto contained more 40 dBZ coverage (Table 2). Their trends in area differ when considering both reflectivity thresholds (Figure 3 and Table 3). Jeanne featured a long and steady increase in 20 dBZ until 33 h after landfall with areas increasing at 232 and 836 sq. km·hr^{-1} (Table 3). Yet, its 40 dBZ regions were fairly small until 8.5 hours after landfall, and later, increases did not exhibit a linear trend. Both 20 and 40 dBZ regions lost area between change points 2 and 3. Humberto experienced a decrease in area during RI, but large increases occurred between points 1 and 2. Figure 4 shows both storms at seven hours after landfall when 40 dBZ coverage was the most contrasting; yet, 20 dBZ coverage was more similar. Despite the similar coverage, the 20 dBZ regions exhibited different spatial patterns. While Humberto's eye was exposed on the south side, Jeanne's eye was completely surrounded by reflectivity values. The majority of Humberto's rain field was located east of the center in the downshear direction. Jeanne's main 20 dBZ region encircled the center out to an average distance of 150 km, with a dry slot evident toward the west. Smaller regions of reflectivity occurred 350 km southeast of the center. These observations demonstrate that examining area alone does not convey important spatial differences in rain field structures.

Turning to the spatial metrics, we first examine closure (Figure 5(a)). Closure was higher for Jeanne when considering 20 dBZ regions around landfall time as expected, but higher for Humberto when considering 40 dBZ regions (Table 2), which was not expected. The higher closure values for Humberto's 40 dBZ regions may be associated with strong convergence during RI, smaller size, and increased moisture availability when compared to Jeanne. The difference in closure is visualized well in Figure 4. When considering the final twelve hours of observations in each storm, closure was higher for both regions in Humberto,

Table 1: Results of Wilcoxon rank sum tests for atmospheric conditions and storm size for data aligned according to time of landfall.

Condition	Level	n	Z	p value	Larger values
Specific humidity	1000–900 hPa	19	−3.7	<0.00	Jeanne
Specific humidity	850–700 hPa	19	−3.82	<0.00	Humberto
Specific humidity	700–500 hPa	19	−3.82	<0.00	Humberto
Specific humidity	500–300 hPa	19	−3.82	<0.00	Humberto
Vertical wind shear speed	200–850 hPa	19	−3.82	<0.00	Humberto
Radius of outermost closed isobar		5	−2.02	0.04	Jeanne
Radius of gale-force winds	All quadrants show the same result	10	−2.81	0.01	Jeanne
Radius of maximum wind		5	−1.75	0.08	Jeanne
Minimum central pressure		10	−2.81	0.01	Humberto

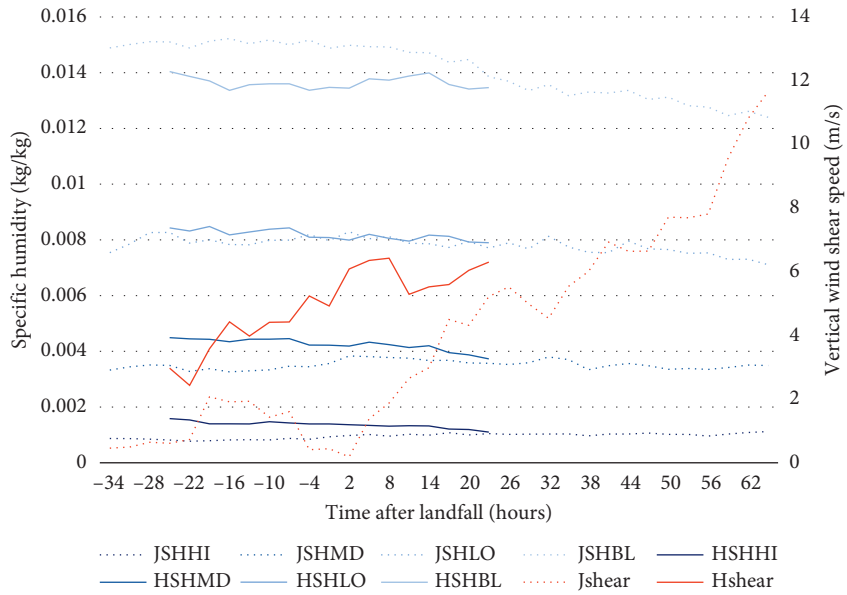

Figure 2: Comparison of specific humidity (SH) averaged across four ranges of altitude (boundary layer (BL), 850–700 hPa (LO), 750–500 hPa (MD), and 500–300 hPa (HI)) and deep-layer vertical wind shear for Jeanne (J) and Humberto (H).

Table 2: Results of Wilcoxon rank sum tests for reflectivity regions aligned by time of landfall from observation start time until twelve hours after landfall (time: landfall) and aligned according to the last 12 hours of available observations (time: end).

Metric	Reflectivity (dBZ)	Time	n	Z	p value	Larger values
Area	20	Landfall	93	−1.57	0.12	
Area	40	Landfall	93	−7.27	<0.00	Humberto
Closure	20	Landfall	93	−7.72	<0.00	Jeanne
Closure	40	Landfall	93	−3.93	<0.00	Humberto
Dispersion	20	Landfall	93	−8.37	<0.00	Humberto
Dispersion	40	Landfall	93	−2.95	<0.00	Humberto
Area	20	End	73	−7.32	<0.00	Jeanne
Area	40	End	73	−0.05	0.96	
Closure	20	End	73	−2.85	<0.00	Humberto
Closure	40	End	73	−4.34	<0.00	Humberto
Dispersion	20	End	73	−3.94	<0.00	Jeanne
Dispersion	40	End	73	−4.89	<0.00	Jeanne

likely due to the fact that this period contains the peak or near-peak values in closure following the RI for Humberto, while Jeanne's reflectivity regions spread radially along the frontal boundary as extratropical transition was occurring.

Jeanne's main 20 dBZ region completely encircled the eye for 17 hours after landfall (Figure 5(a)). This is the time of the first change point (Table 4), when the center started to become exposed on the south side at a rate of 5.6 hr^{-1}.

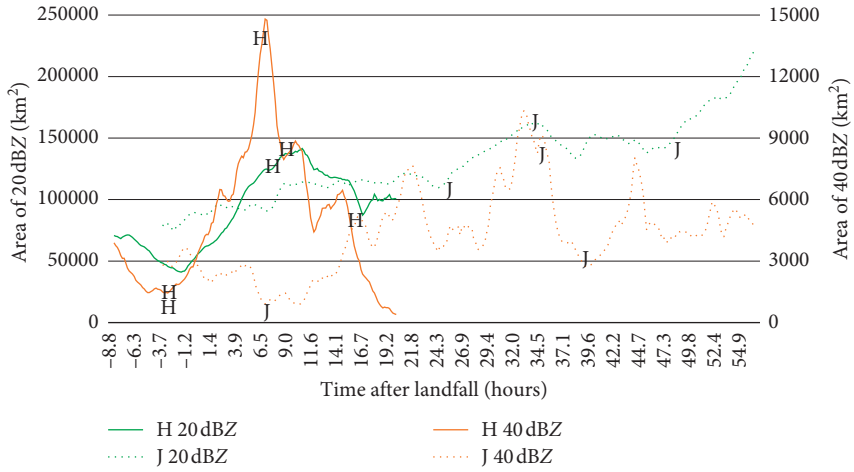

Figure 3: Areas occupied by all 20 and 40 dBZ polygons for Humberto (H) and Jeanne (J) aligned by time after landfall. Letters correspond to change points in Table 3.

Table 3: Results of change point analysis for areas of 20 and 40 dBZ regions with time of change point in hours after landfall, slope of trend line in between each change point in sq. km·hr^{-1}, and the coefficient of determination for each trend line.

	J 20 area	J 40 area	H 20 area	H 40 area
Change point 1	26.5	8.5	−1.5	−1.4
Change point 2	32.8	35.7	9.2	7.3
Change point 3	47.1	36.9	17	8.2
Slope 1	232	−28	−872	−42
Slope 2	836	43	1663	232
Slope 3	−177	−652	−1039	−887
Slope 4	1269	13	70	−127
R^2 1	0.82	0.59	0.96	0.55
R^2 2	0.99	0.67	0.99	0.92
R^2 3	0.30	0.98	0.90	0.99
R^2 4	0.97	0.17	0.02	0.89

This occurred near the time that Jeanne weakened to a tropical storm and the dry slot evident in Figure 4(a) reached the radius of maximum winds. Change points 2 and 3 mark a brief period when Jeanne's center became completely enclosed as a small region of 20 dBZ values developed 15 km south of the center but then dissipated so that exposure proceeded at a rate of 11.9 hr^{-1}. Jeanne's 40 dBZ regions reduced in closure until 9.5 hours after landfall (Figure 5(a)). This reduction began prior to attaining maximum intensity and may be the result of moving through an environment containing less moisture as compared to Humberto (Figure 2). Change point 2 for the 40 dBZ regions coincided with change point 1 of the 20 dBZ regions, and the decrease in closure occurred at a similar rate for a similar length of time. This indicates that the processes responsible for the decrease in closure, which include weakening of the primary circulation and increasing vertical wind shear, were affecting both the stratiform and convective regions in a similar manner. However, little change in closure occurred for the remainder of 40 dBZ observations despite increases and decreases in 20 dBZ regions. This may be attributed to interaction with the warm front helping to increase stratiform precipitation, but not convective precipitation.

The trends in closure between the 20 and 40 dBZ regions match well for Humberto (Table 4) despite covering a different range of values (Figure 5(a)). The RI period coincided with increased exposure at a rate of 25 hr^{-1}, which is contrary to the hypothesized increase in closure. This difference is likely explained by the lag in time needed for the convergence of angular momentum to increase the tangential winds by 13 m·s^{-1} over a short six-hour span. This increases the convergence of air, which is followed by uplift, condensation, and precipitation. This idea is supported by the fact that closure increased beginning less than two hours later at an even faster rate of 57 and 75 hr^{-1} for 20 and 40 dBZ regions, respectively. Thus, we find a six-hour offset between time of maximum intensity and complete enclosure of the circulation center. Maximum tangential extent of 40 dBZ regions occurred 6 hours later, suggesting a 12-hour lag for these regions located farther from the circulation center. At this point, 40 dBZ regions continued to spread tangentially for five more hours at a much slower rate, while the 20 dBZ regions completely enclosed the center over the next four hours before decreasing in coverage as did the 40 dBZ regions. During this period, shear continued to increase as Humberto interacted with the stationary front.

Both storms became less dispersed as they intensified before landfall, and then, dispersion generally increased thereafter (Figure 5(b)). Despite its smaller size, Humberto was more dispersed at the beginning (Table 2), which could be attributed to its lower intensity and higher values of shear. For Humberto, the change point analysis identified 6.5 and 3 hours before landfall as the point where slope changes from −33 and −39 km·hr^{-1} to −3 and 9 km·hr^{-1} for 20 and 40 dBZ regions, respectively (Table 5). This period is aligned with that of RI. Subsequent increases in dispersion occurred when vertical wind shear was also increasing to moderate strength. The decreasing trend in the 40 dBZ regions for Slope 4 was likely due to the rapid decrease in areal coverage (Figure 3). Jeanne had higher values of dispersion when the last

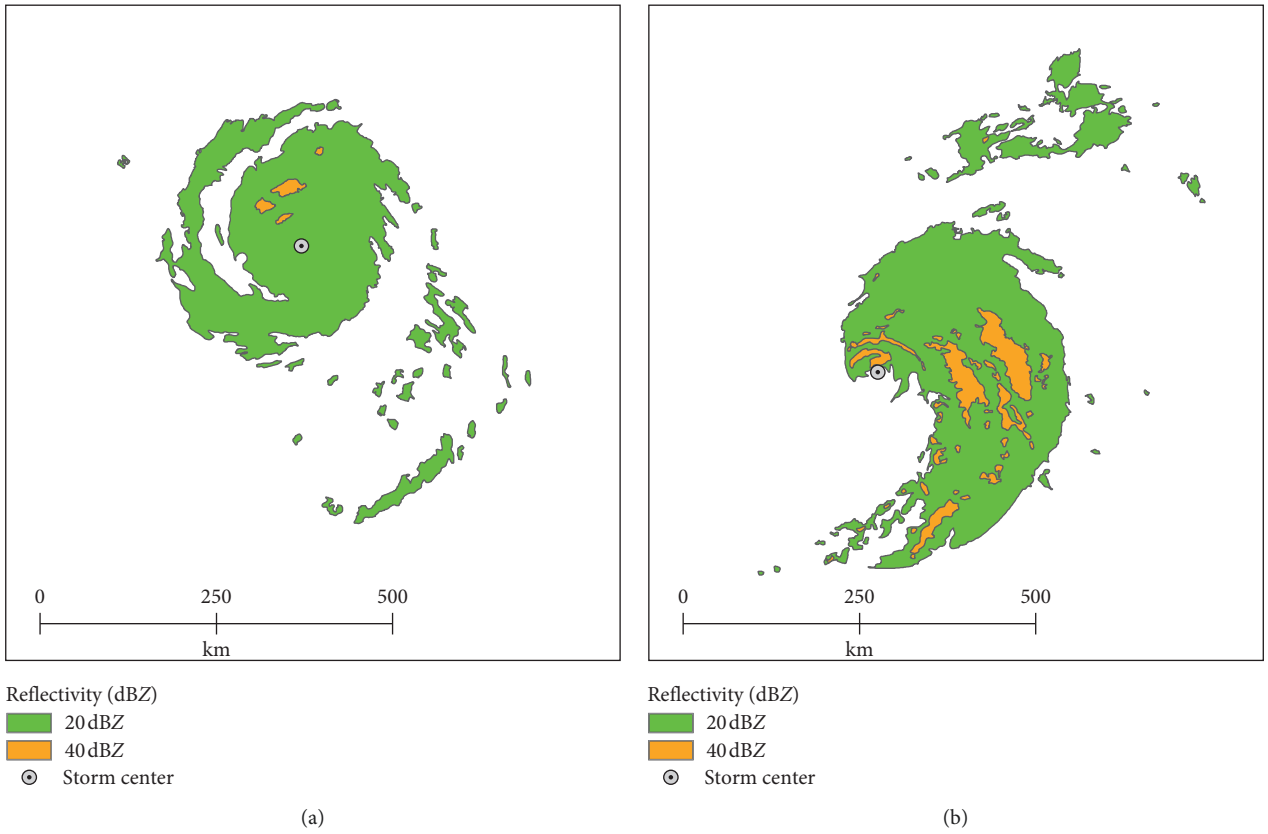

Figure 4: Reflectivity regions of 20 and 40 dBZ at seven hours after landfall for (a) Jeanne and (b) Humberto.

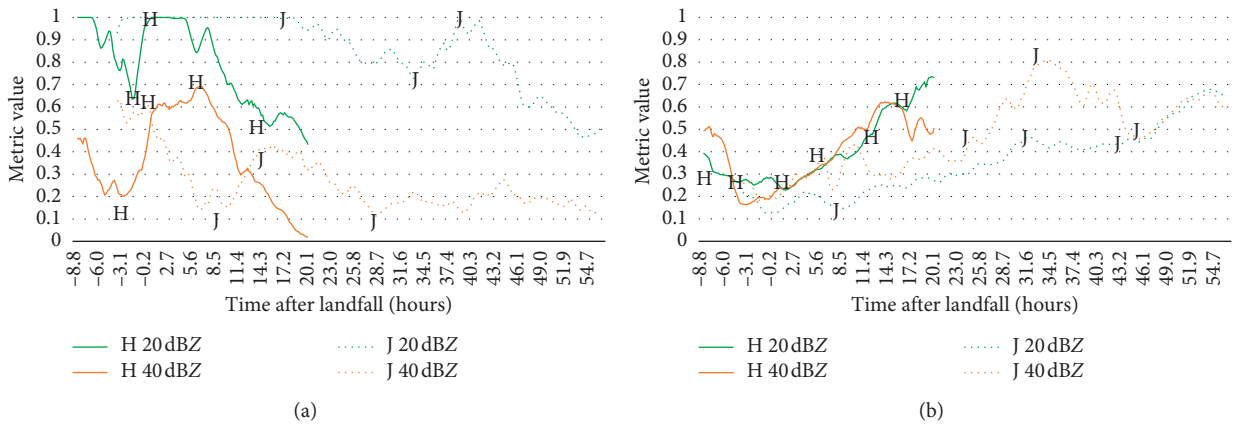

Figure 5: Values of (a) closure and (b) dispersion for all 20 and 40 dBZ polygons for Humberto (H) and Jeanne (J) aligned by time after landfall. Letters correspond to change points in Tables 4 and 5.

12 hours of observations are compared (Table 2) as reflectivity expanded radially along the warm front as shear increased (Figure 2). For Jeanne's 20 dBZ regions, all trends were positive, but dispersion increased more slowly than for Humberto. Change points 2 and 3 occurred near the same time for 20 and 40 dBZ regions in Jeanne (Table 5, Figure 5(b)); both increased at approximately 10 km·hr^{-1} at the end of the observation period and covered the same range of values. This coincided with the time that vertical wind shear increased to moderate strength (Figure 2).

The calculation of displacement toward the east and north utilizes the same equation as for dispersion, save for adding a cosine (equation (3)) and sine (equation (4)) component to provide a combined radial and tangential measure of where the centroids of the main rainfall regions are located [52]:

Table 4: Results of change point analysis for closure of 20 and 40 dBZ regions with time of change point in hours after landfall, slope of trend line in between each change point in hr^{-1}, and the coefficient of determination for each trend line.

	J 20 close	J 40 close	H 20 close	H 40 close
Change point 1	17	9.5	−1.3	−2.2
Change point 2	33.5	14.8	1.3	1.5
Change point 3	38.5	27.3	14.5	6.7
Slope 1	0.13	−14.69	−25.8	−24
Slope 2	−5.62	21.6	72	57
Slope 3	16	−7.78	−19.5	6.6
Slope 4	−11.88	0.01	−6.3	−26.4
R^2 1	0.03	0.79	0.61	0.58
R^2 2	0.81	0.84	0.79	0.83
R^2 3	0.63	0.75	0.86	0.25
R^2 4	0.91	0.004	0.13	0.96

$$DisN = \sum_{i=1}^{NP} \frac{\text{area}_i}{\sum_j^{NP} \text{area}_j} \left(\frac{r_{\text{centroid},i}}{r_{\text{search}}} \right) \cos\ \theta_i, \quad (3)$$

$$DisE = \sum_{i=1}^{NP} \frac{\text{area}_i}{\sum_j^{NP} \text{area}_j} \left(\frac{r_{\text{centroid},i}}{r_{\text{search}}} \right) \sin\ \theta_i. \quad (4)$$

We visualize these values on a scatter plot with the circulation center at 0, 0 (Figure 6). Jeanne's centroids began west of the center which was the forward quadrant of the storm. The main 20 dBZ region was aligned with the center at landfall (Figure 6(a)) and remained within 50 km of the center for ten more hours. At this point, drier air eroded precipitation south of center and the centroid shifted north. At 24 hours after landfall, the centroid shifted northeast as the southwesterly shear increased to moderate strength. During the last 24 hours, the shift was predominantly north, parallel to the frontal boundary. The 40 dBZ regions (Figure 6(c)) were more prevalent in the relatively thin outer rainbands northeast of the storm's center (Figure 1) rather than along the warm front.

By contrast, Humberto's 20 (Figure 6(b)) and 40 dBZ (Figure 6(d)) centroids were always more than 50 km away from center as the rainfall never developed west of the eyewall. The overall trend in motion was primarily east in the downshear direction. However, a trend inward toward the storm center happened during the RI period. The move away from the center then occurred differently in the 20 and 40 dBZ regions. More 40 dBZ regions were east of the center in the thin outer rainbands rather than along the stationary front boundary northeast where the 20 dBZ regions were concentrated.

Looking at the Spearmen's rank correlation coefficients, values are higher in general for Jeanne than for Humberto, which is likely due to a more gradual weakening and transition into an extratropical system for Jeanne, whereas Humberto intensified and weakened faster. In both storms, dispersion and closure are inversely correlated while dispersion and area are positively correlated, but these relationships are weak for Humberto's 40 dBZ regions. The largest difference between the storms occurs when comparing closure and area for 40 dBZ regions. These variables are positively correlated in Humberto but inversely correlated in Jeanne. This indicates that when 40 dBZ regions were larger, they tended to encircle Humberto's center while for Jeanne, they did not.

Although the correlation analyses show an inverse relationship between dispersion and closure (Tables 6 and 7), examining the timing of changes in slope and the directions of the slopes reveals that dispersion and closure can have a positive association. The best examples of this occurred around change point 1 in Humberto's 20 and 40 dBZ regions. Closure changed quicker than dispersion so that the change points did not align precisely in time, but both metrics decreased strongly in Slope 1 (Tables 4 and 5). Humberto's 40 dBZ regions then increased sharply in closure during Slope 2, and 40 dBZ dispersion also increased. Another observation that can be made concerns the timing of the change points. Closure tended to have more change points earlier in the time series than dispersion (Tables 4 and 5). This occurred at all 20 and 40 dBZ times for Humberto, and half of the times for Jeanne. Thus, closure may be more sensitive than dispersion to subtle changes in environmental conditions, particularly as the storm's core experiences the entrainment of dry air and erodes. Thus, both metrics provide unique information to gain a more full understanding of structural changes in TC rain fields.

By adjusting the search radius, we can consider reflectivity regions located at any distance range from the circulation center. Previous researchers have used 50–162 km from the center to delineate the inner core of a TC while designating rainfall 350–500+ km as belonging to the outer region [53, 54]. For simplicity, we only discuss the results for closure, which we recalculated for regions ranging every 100 km outward from the circulation center to 500 km. Other distances could be utilized such as those that correspond to R17 or ROCI for a given storm or basin-wide averages of these values such as those reported in Kimball and Mulekar [55].

Figure 7 displays closure as previously calculated over 0–500 km in a black dotted line and the new calculation for 0–100 km in a solid black line to emphasize that closure was mainly dictated by processes operating in the storm's core at the beginning of the observations. The other distances are represented in progressively lighter shades to emphasize the increase in distance away from the storm center as the primary and secondary circulations weakened and the main focus of convergence shifted to the area along the frontal boundary and the outer rainbands. For 20 dBZ regions, Jeanne's core (0–100 km) became greatly exposed for 24–36 hours after landfall, but overall closure remained high due to the reflectivity regions 100–200 km from the center (Figure 7(a)). A clear difference is seen when comparing the inner core regions 0–100 and 100–200 km from the center and the outer regions located 300–400 and 400–500 km from the center, with 200–300 km splitting the difference. For Humberto's 20 dBZ regions (Figure 7(b)), the inner core dominated the closure value until 12 hours after landfall. The importance of reflectivity increasing along the stationary front became evident in increasing closure values after

Table 5: Results of change point analysis for dispersion of 20 and 40 dBZ regions with time of change point in hours after landfall, slope of trend line in between each change point in km·hr^{-1}, and the coefficient of determination for each trend line.

	J 20 disperse	J 40 disperse	H 20 disperse	H 40 disperse
Change point 1	9.2	24.2	−6.5	−3
Change point 2	32.2	33.5	2.2	5.3
Change point 3	43.3	44.8	9.7	14
Slope 1	0.15	3.3	−33	−39
Slope 2	5.4	21.9	−3	9
Slope 3	0.15	−14.1	10.5	18
Slope 4	10.2	9	16.8	−12.9
R^2 1	0.001	0.54	0.95	0.9
R^2 2	0.91	0.94	0.54	0.97
R^2 3	0.001	0.83	0.95	0.98
R^2 4	0.92	0.73	0.93	0.64

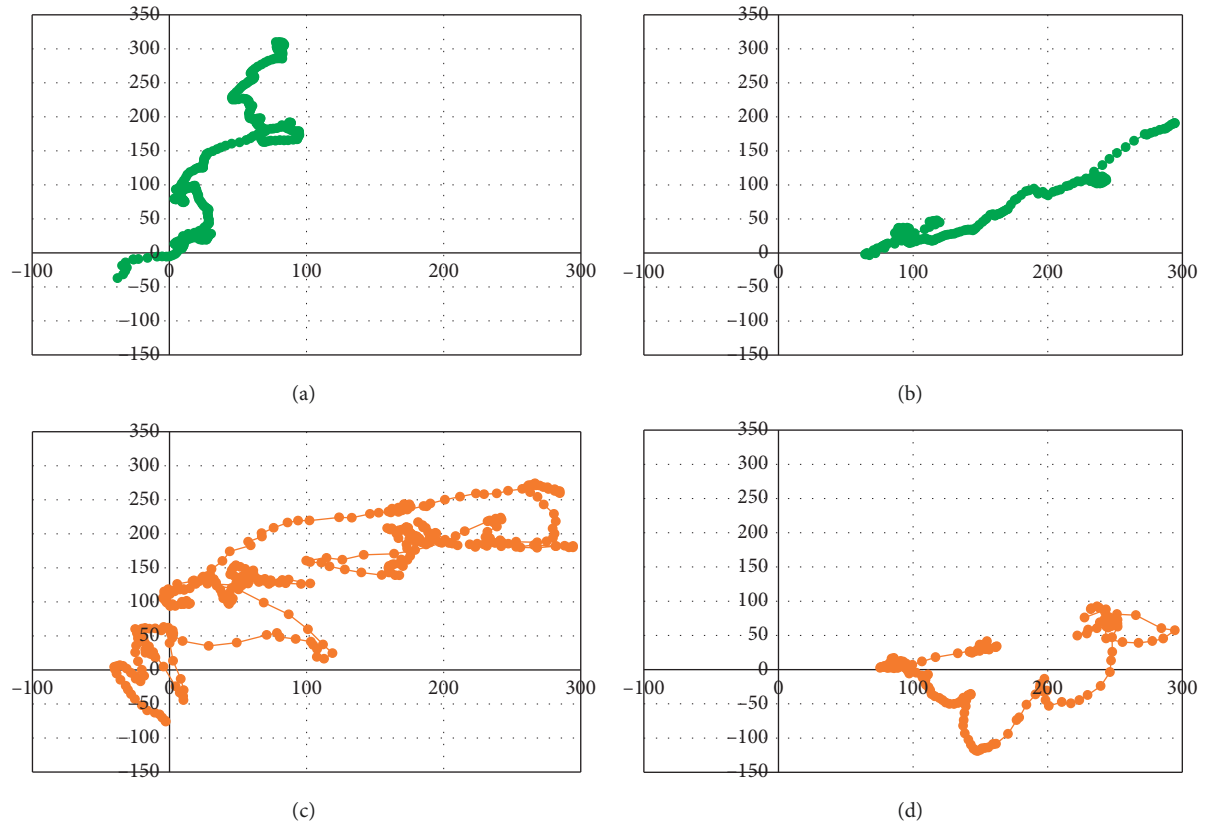

Figure 6: Displacement (km) from the storm center (located at 0, 0) at each observation time for (a) Jeanne 20 dBZ, (b) Humberto 20 dBZ, (c) Jeanne 40 dBZ, and (d) Humberto 40 dBZ regions. Positive Y-axis extends to the north, and positive X-axis extends to the east.

landfall from 200 to 500 km outward from the storm center as moisture was sourced from over-ocean and rose over the front oriented perpendicular to the flow. In Jeanne, 40 dBZ values beyond 100 km accounted for most of closure after 20 hours after landfall as little convection remained in the core (Figure 7(c)). The development of convection at 100–200 and then 200–300 km helped to increase closure for Humberto's 40 dBZ regions for the first 12 hours after landfall (Figure 7(d)). These findings reveal how adjusting the search radius facilitates investigation of processes occurring in different regions of the storm that contribute to overall rainfall production.

4. Conclusions and Future Work

This study examined changes in the tangential and radial distributions of radar reflectivity regions in two landfalling hurricanes, demonstrating that they provide important spatial information that should be considered in addition to areal coverage. We created a 3D mosaic of reflectivity data from the WSR-88D network and extracted values along a constant altitude of 3.5 km. At 10-minute intervals, we used a GIS to contour regions of reflectivity greater than or equal to 20 and 40 dBZ and converted these regions into polygons. We analyzed polygons whose centroids fell within a 500 km

Table 6: Coefficients from Spearman's rank correlation tests comparing dispersion, closure, and area for 20 and 40 dBZ regions in Jeanne. All values are statistically significant at the 0.01 level.

	J 20 C	J 20 A	J 40 D	J 40 C	J 40 A
J 20 D	−0.93	0.93	0.82	−0.60	0.67
J 20 C	—	−0.87	−0.77	0.59	−0.71
J 20 A		—	0.89	−0.65	0.67
J 40 D			—	−0.75	0.58
J 40 C				—	−0.17

Table 7: Coefficients from Spearman's rank correlation tests comparing dispersion, closure, and area for 20 and 40 dBZ regions in Humberto.

	H 20 C	H 20 A	H 40 D	H 40 C	H 40 A
H 20 D	−0.75	0.64	0.88	−0.44	−0.02
H 20 C	—	−0.32	−0.56	0.73	0.29
H 20 A		—	0.65	0.29	0.67
H 40 D			—	−0.30	0.10
H 40 C				—	0.83

The two values in italics are not statistically significant at the 0.01 level.

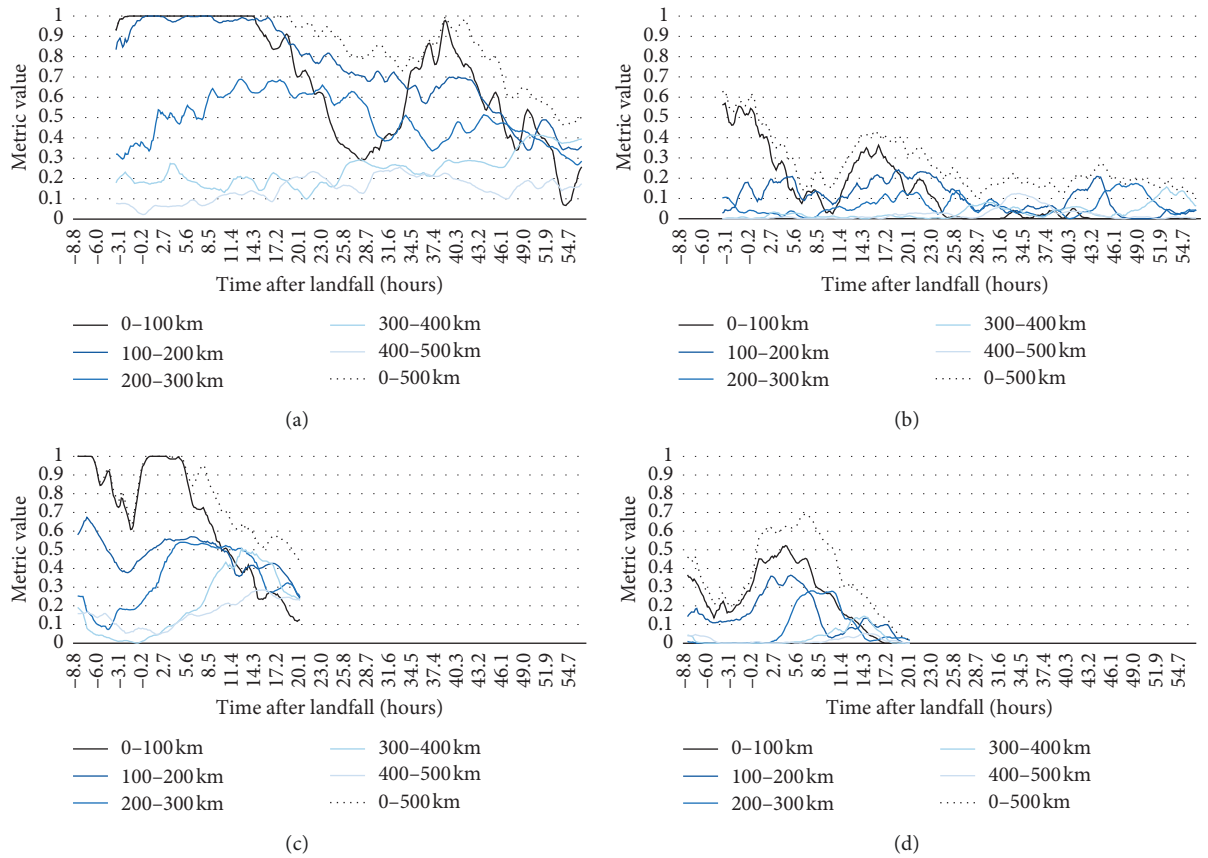

Figure 7: Closure values calculated over six ranges outward from the circulation center (km) for (a) Jeanne 20 dBZ, (b) Jeanne 40 dBZ, (c) Humberto 20 dBZ, and (d) Humberto 40 dBZ regions. Stippled black lines correspond to the same lines in Figure 5.

radius of the storm center. We calculated the area occupied by each polygon and its distance and bearing relative to the storm center. We then calculated values of closure, or the tangential completeness of reflectivity regions surrounding the circulation center, and dispersion, or the spread of reflectivity regions outwards from the storm center. We also calculated displacement to provide a combined radial and tangential component to the location of the main rainfall regions. Additionally, we demonstrate the flexibility of our metrics by considering different ranges of search radii.

Our results indicate that by calculating these metrics at a high spatial and temporal resolution, it is possible to detect

more subtle and shorter-term changes in rainband structures than would be possible using more coarse datasets. Changes in closure occurred closer to the time of maximum intensity and landfall than did dispersion or area despite the strong and statistically significant correlation coefficients between the variables. The correlation analyses showed that dispersion and area tend to have a positive association while closure tends to have a negative association with dispersion. But, a closer examination with the change point analysis revealed that closure and dispersion were positively related during Humberto's RI.

The metrics reveal contrasting patterns of response to slower intensification and then weakening in Jeanne versus RI and faster weakening in Humberto. The slopes of the trend lines were higher for Humberto than Jeanne, which is likely due to differences in rates of intensification and velocity of wind shear experienced by each storm. Jeanne's eye was completely surrounded by 20 dBZ values for 17 hours after landfall and during the majority of this time, closure decreased for its 40 dBZ regions. In contrast, Humberto's inner core only began to more fully enclose the circulation center at the end of the RI period, revealing a six-hour offset between time of maximum intensity and complete closure near the circulation center and a 12-hour lag for reflectivity regions located farther outward. Closure increased despite the increasing shear as well, indicating that in a smaller storm such as Humberto, inner-core processes can withstand an increasingly hostile environment when moisture is high. The growth in area for Humberto's 40 dBZ regions after landfall along with increasing dispersion also demonstrates the rate with which the increased convergence from the primary circulation eventually helps to increase convergence radially outward from the circulation center.

Our analysis also revealed differences in rain field organization as each TC interacted with a frontal boundary. Jeanne's reflectivity regions were more dispersed along the warm front, and 20 dBZ regions occupied a greater area than those of Humberto. Perhaps, due to a smaller radius of maximum winds, closure was higher for Humberto during the last 12 hours of observations when compared to Jeanne. Changes in the trends of area, dispersion, and closure tended to occur later in Jeanne's observations than for Humberto. This indicates that rainband structure exhibited more changes as the process of extratropical transition began for Jeanne than when making landfall and weakening from a major hurricane to a tropical storm.

In addition to examining additional TCs to determine how generalizable the trends discovered in this study are, future work will more closely examine the role of moisture in the evolution of TC rainfall regions. Matyas [56] and Takakura et al. [57] discuss the importance of moisture advection for rain rates in TCs, and Matyas et al. [19] show how dry air wrapped around the circulation of Hurricane Isabel (2003) during extratropical transition. We aim to trace the advection of dry air into the core of the storm and expand our search radius more than 1500 km to measure the extent of the deep tropical moisture that is advected into some TCs as they approach land.

The dispersion of TC rain fields during their entire life cycle has been calculated utilizing data from NARR [9]. However, the relatively coarse spatial resolution of the NARR data did not permit the analysis of closure to capture processes in the eyewall. Thus, we will analyze area, closure, dispersion, and displacement over a large sample of TCs and utilize a variety of search radii to compare results according to storm size as indicated by the wind fields and rainfall extent [58, 59]. In addition to using data from ground-based radars, we will analyze high-resolution data available from Geostationary Operational Environmental Satellite 16 to enable analysis from formation to dissipation. We can also utilize our metrics to compare rain-filled regions as detected by both ground-based and space-borne sensors so that continuous monitoring can occur in the absence of one of the platforms.

Data Availability

The data pertaining to the hurricane tracks, radar reflectivity values, NARR, and extended best track (EBT) were all obtained from publically available websites. Storm tracks: http://www.aoml.noaa.gov/hrd/hurdat/hurdat2.html; radar: https://www.ncdc.noaa.gov/nexradinv/; NARR: https://www.esrl.noaa.gov/psd/data/narr/; and EBT: http://rammb.cira.colostate.edu/research/tropical_cyclones/tc_extended_best_track_dataset/. Codes for calculations are available on GitHub at https://github.com/striges/RadarComposite and https://github.com/striges/wrf_radar_project_mp.

Conflicts of Interest

The authors declare that there are no conflicts of interest regarding the publication of this paper.

Acknowledgments

This research was funded through the University of Florida Research Opportunity Fund and a CAREER award from the National Science Foundation (BCS 1053864).

References

[1] E. N. Rappaport, "Fatalities in the United States from Atlantic tropical cyclones—new data and interpretation," *Bulletin of the American Meteorological Society*, vol. 95, no. 3, pp. 341–346, 2014.

[2] D. Kim, C.-H. Ho, D.-S. R. Park, J. C. L. Chan, and Y. Jung, "The relationship between tropical cyclone rainfall area and environmental conditions over the subtropical oceans," *Journal of Climate*, vol. 31, no. 12, pp. 4605–4616, 2018.

[3] P. Lu, N. Lin, K. Emanuel, D. Chavas, and J. Smith, "Assessing hurricane rainfall mechanisms using a physics-based model: hurricanes Isabel (2003) and Irene (2011)," *Journal of the Atmospheric Sciences*, vol. 75, no. 7, pp. 2337–2358, 2018.

[4] M. F. Rios Gaona, G. Villarini, W. Zhang, and G. A. Vecchi, "The added value of IMERG in characterizing rainfall in tropical cyclones," *Atmospheric Research*, vol. 209, pp. 95–102, 2018.

[5] N. Lin, J. A. Smith, G. Villarini, T. P. Marchok, and M. L. Baeck, "Modeling extreme rainfall, winds, and surge from hurricane Isabel (2003)," *Weather and Forecasting*, vol. 25, no. 5, pp. 1342–1361, 2010.

[6] C. J. Matyas, "Conditions associated with large rain-field areas for tropical cyclones landfalling over Florida," *Physical Geography*, vol. 35, no. 2, pp. 93–106, 2014.

[7] N. Nasrollahi, A. AghaKouchak, J. Li, X. Gao, K. Hsu, and S. Sorooshian, "Assessing the impacts of different WRF precipitation physics in hurricane simulations," *Weather and Forecasting*, vol. 27, no. 4, pp. 1003–1016, 2012.

[8] J. A. Knaff, J. P. Kossin, and M. DeMaria, "Annular hurricanes," *Weather and Forecasting*, vol. 18, no. 2, pp. 204–223, 2003.

[9] S. E. Zick and C. J. Matyas, "A shape metric methodology for studying the evolving geometries of synoptic-scale precipitation patterns in tropical cyclones," *Annals of the American Association of Geographers*, vol. 106, no. 6, pp. 1217–1235, 2016.

[10] K. L. Corbosiero and J. Molinari, "The effects of vertical wind shear on the distribution of convection in tropical cyclones," *Monthly Weather Review*, vol. 130, no. 8, pp. 2110–2123, 2002.

[11] M. Lonfat, R. Rogers, T. Marchok, and F. D. Marks, "A parametric model for predicting hurricane rainfall," *Monthly Weather Review*, vol. 135, no. 9, pp. 3086–3097, 2007.

[12] C. J. Matyas, "A geospatial analysis of convective rainfall regions within tropical cyclones after landfall," *International Journal of Applied Geospatial Research*, vol. 1, no. 2, pp. 71–91, 2010.

[13] W. Xu, H. Jiang, and X. Kang, "Rainfall asymmetries of tropical cyclones prior to, during, and after making landfall in south China and southeast United States," *Atmospheric Research*, vol. 139, pp. 18–26, 2014.

[14] K. A. Hill and G. M. Lackmann, "Influence of environmental humidity on tropical cyclone size," *Monthly Weather Review*, vol. 137, no. 10, pp. 3294–3315, 2009.

[15] C. J. Matyas and M. Cartaya, "Comparing the rainfall patterns produced by hurricanes Frances (2004) and Jeanne (2004) over Florida," *Southeastern Geographer*, vol. 49, no. 2, pp. 132–156, 2009.

[16] S. A. Braun, J. A. Sippel, and D. S. Nolan, "The impact of dry midlevel air on hurricane intensity in idealized simulations with no mean flow," *Journal of the Atmospheric Sciences*, vol. 69, no. 1, pp. 236–257, 2012.

[17] Y. Ying and Q. Zhang, "A modeling study on tropical cyclone structural changes in response to ambient moisture variations," *Journal of the Meteorological Society of Japan*, vol. 90, no. 5, pp. 755–770, 2012.

[18] S. K. Kimball, "Structure and evolution of rainfall in numerically simulated landfalling hurricanes," *Monthly Weather Review*, vol. 136, no. 10, pp. 3822–3847, 2008.

[19] C. J. Matyas, S. E. Zick, and J. Tang, "Using an object-based approach to quantify the spatial structure of reflectivity regions in hurricane Isabel (2003). Part I: comparisons between radar observations and model simulations," *Monthly Weather Review*, vol. 146, no. 5, pp. 1319–1340, 2018.

[20] Q. Tang, L. Xie, G. M. Lackmann, and B. Liu, "Modeling the impacts of the large-scale atmospheric environment on inland flooding during the landfall of hurricane Floyd (1999)," *Advances in Meteorology*, vol. 2013, Article ID 294956, 16 pages, 2013.

[21] E. Atallah, L. F. Bosart, and A. R. Aiyyer, "Precipitation distribution associated with landfalling tropical cyclones over the eastern United States," *Monthly Weather Review*, vol. 135, no. 6, pp. 2185–2206, 2007.

[22] E. A. Ritchie and R. L. Elsberry, "Simulations of the transformation stage of the extratropical transition of tropical cyclones," *Monthly Weather Review*, vol. 129, no. 6, pp. 1462–1480, 2001.

[23] V. F. Dvorak, "Tropical cyclone intensity analysis and forecasting from satellite imagery," *Monthly Weather Review*, vol. 103, no. 5, pp. 420–430, 1975.

[24] V. F. Dvorak, *A Workbook on Tropical Clouds and Cloud Systems Observed in Satellite Imagery*, US Dept. of Commerce, National Oceanic and Atmospheric Administration, National Environmental Satellite Data, and Information Service, and National Weather Service, Washington, DC, USA, 1982.

[25] G. M. Barnes, J. F. Gamache, M. A. Lemone, and G. J. Stossmeister, "A convective cell in a hurricane rainband," *Monthly Weather Review*, vol. 119, no. 3, pp. 776–794, 1991.

[26] D. A. Hence and R. A. Houze, "Vertical structure of tropical cyclone rainbands as seen by the TRMM precipitation radar," *Journal of the Atmospheric Sciences*, vol. 69, no. 9, pp. 2644–2661, 2012.

[27] H. E. Willoughby, "Temporal changes of the primary circulation in tropical cyclones," *Journal of the Atmospheric Sciences*, vol. 47, no. 2, pp. 242–264, 1990.

[28] H. Riehl, "A model of hurricane formation," *Journal of Applied Physics*, vol. 21, no. 9, pp. 917–925, 1950.

[29] M. Croxford and G. M. Barnes, "Inner core strength of Atlantic tropical cyclones," *Monthly Weather Review*, vol. 130, no. 1, pp. 127–139, 2002.

[30] G. J. Holland and R. T. Merrill, "On the dynamics of tropical cyclone structural changes," *Quarterly Journal of the Royal Meteorological Society*, vol. 110, no. 465, pp. 723–745, 1984.

[31] OFCM, "Federal meteorological handbook, No. 11: WSR-88D meteorological observations. Part C WSR-88D products and algorithms," Technical Report, FCM-H11C-2017, Office of the Federal Coordinator for Meteorological Services and Supporting Research, Silver Spring, MD, USA, 2017.

[32] J. L. Franklin, R. J. Pasch, L. A. Avila et al., "Atlantic hurricane season of 2004," *Monthly Weather Review*, vol. 134, no. 3, pp. 981–1025, 2006.

[33] M. J. Brennan, R. D. Knabb, M. Mainelli, and T. B. Kimberlain, "Atlantic hurricane season of 2007," *Monthly Weather Review*, vol. 137, no. 12, pp. 4061–4088, 2009.

[34] E. N. Rappaport, J. L. Franklin, A. B. Schumacher, M. DeMaria, L. K. Shay, and E. J. Gibney, "Tropical cyclone intensity change before U.S. Gulf coast landfall," *Weather and Forecasting*, vol. 25, no. 5, pp. 1380–1396, 2010.

[35] C. W. Landsea and J. L. Franklin, "Atlantic hurricane database uncertainty and presentation of a new database format," *Monthly Weather Review*, vol. 141, no. 10, pp. 3576–3592, 2013.

[36] V. Lakshmanan and T. W. Humphrey, "A MapReduce technique to mosaic continental-scale weather radar data in real-time," *IEEE Journal of Selected Topics in Applied Earth Observations and Remote Sensing*, vol. 7, no. 2, pp. 721–732, 2014.

[37] J. Tang and C. J. Matyas, "Fast playback framework for analysis of ground-based doppler radar observations using MapReduce technology," *Journal of Atmospheric and Oceanic Technology*, vol. 33, no. 4, pp. 621–634, 2016.

[38] M. Steiner, R. A. Houze, and S. E. Yuter, "Climatological characterization of three-dimensional storm structure from

operational radar and rain gauge data," *Journal of Applied Meteorology*, vol. 34, no. 9, pp. 1978–2007, 1995.

[39] D. F. Jorgensen, "Mesoscale and convective-scale characteristics of mature hurricanes. Part I: general observations by research aircraft," *Journal of the Atmospheric Sciences*, vol. 41, no. 8, pp. 1268–1286, 1984.

[40] J. Larson, Y. Zhou, and R. W. Higgins, "Characteristics of landfalling tropical cyclones in the United States and Mexico: climatology and interannual variability," *Journal of Climate*, vol. 18, no. 8, pp. 1247–1262, 2005.

[41] G. Villarini, R. Goska, J. A. Smith, and G. A. Vecchi, "North Atlantic tropical cyclones and U.S. flooding," *Bulletin of the American Meteorological Society*, vol. 95, no. 9, pp. 1381–1388, 2014.

[42] C. Matyas, "Quantifying the shapes of U.S. landfalling tropical cyclone rain shields∗," *Professional Geographer*, vol. 59, no. 2, pp. 158–172, 2007.

[43] P. A. Harr and R. L. Elsberry, "Extratropical transition of tropical cyclones over the western North Pacific. Part I: evolution of structural characteristics during the transition process," *Monthly Weather Review*, vol. 128, no. 8, pp. 2613–2633, 2000.

[44] S. C. Jones, P. A. Harr, J. Abraham et al., "The extratropical transition of tropical cyclones: forecast challenges, current understanding, and future directions," *Weather and Forecasting*, vol. 18, no. 6, pp. 1052–1092, 2003.

[45] P. M. Klein, P. A. Harr, and R. L. Elsberry, "Extratropical transition of western North Pacific tropical cyclones: an overview and conceptual model of the transformation stage," *Weather and Forecasting*, vol. 15, no. 4, pp. 373–395, 2000.

[46] F. Mesinger, G. DiMego, E. Kalnay et al., "North American regional reanalysis," *Bulletin of the American Meteorological Society*, vol. 87, no. 3, pp. 343–360, 2006.

[47] S. E. Zick and C. J. Matyas, "Tropical cyclones in the North American regional reanalysis: the impact of satellite-derived precipitation over ocean," *Journal of Geophysical Research: Atmospheres*, vol. 120, no. 17, pp. 8724–8742, 2015.

[48] M. DeMaria, M. Mainelli, L. K. Shay, J. A. Knaff, and J. Kaplan, "Further improvements to the statistical hurricane intensity prediction scheme (SHIPS)," *Weather and Forecasting*, vol. 20, no. 4, pp. 531–543, 2005.

[49] F. Wilcoxon, S. Katti, and R. A. Wilcox, "Critical values and probability levels for the Wilcoxon rank sum test and the Wilcoxon signed rank test," in *Selected Tables in Mathematical Statistics*, vol. 1, pp. 171–259, American Mathematical Society, Providence, RI, USA, 1970.

[50] W. M. Frank and E. A. Ritchie, "Effects of environmental flow upon tropical cyclone structure," *Monthly Weather Review*, vol. 127, no. 9, pp. 2044–2061, 1999.

[51] S. C. Jones, "On the ability of dry tropical-cyclone-like vortices to withstand vertical shear," *Journal of the Atmospheric Sciences*, vol. 61, no. 1, pp. 114–119, 2004.

[52] Y. Zhou and C. J. Matyas, "Spatial characteristics of rain fields associated with tropical cyclones landfalling over the western Gulf of Mexico and Caribbean sea," *Journal of Applied Meteorology and Climatology*, vol. 57, no. 8, pp. 1711–1727, 2018.

[53] D. J. Cecil, E. J. Zipser, and S. W. Nesbitt, "Reflectivity, ice scattering, and lightning characteristics of hurricane eyewalls and rainbands. Part I: quantitative description," *Monthly Weather Review*, vol. 130, no. 4, pp. 769–784, 2002.

[54] H. Jiang and E. M. Ramirez, "Necessary conditions for tropical cyclone rapid intensification as derived from 11 years of TRMM data," *Journal of Climate*, vol. 26, no. 17, pp. 6459–6470, 2013.

[55] S. K. Kimball and M. S. Mulekar, "A 15-year climatology of North Atlantic tropical cyclones. Part I: size parameters," *Journal of Climate*, vol. 17, no. 18, pp. 3555–3575, 2004.

[56] C. Matyas, "Comparing the spatial patterns of rainfall and atmospheric moisture among tropical cyclones having a track similar to hurricane Irene (2011)," *Atmosphere*, vol. 8, no. 12, pp. 165–185, 2017.

[57] T. Takakura, R. Kawamura, T. Kawano, K. Ichiyanagi, M. Tanoue, and K. Yoshimura, "An estimation of water origins in the vicinity of a tropical cyclone's center and associated dynamic processes," *Climate Dynamics*, vol. 50, no. 1-2, pp. 555–569, 2018.

[58] Q. Guo and C. J. Matyas, "Comparing the spatial extent of Atlantic basin tropical cyclone wind and rain fields prior to land interaction," *Physical Geography*, vol. 37, no. 1, pp. 5–25, 2016.

[59] Y. Zhou, C. Matyas, H. Li, and J. Tang, "Conditions associated with rain field size for tropical cyclones landfalling over the eastern United States," *Atmospheric Research*, vol. 214, pp. 375–385, 2018.